

See discussions, stats, and author profiles for this publication at: <https://www.researchgate.net/publication/262363783>

An Attenuated Projector for Iterative Reconstruction Algorithm of a High Sensitivity Tomographic Gamma Scanner

Article in IEEE Transactions on Nuclear Science · April 2014

DOI: 10.1109/TNS.2014.2302454

CITATION

1

READS

90

9 authors, including:



[Martín Alberto Belzunce](#)

King's College London

13 PUBLICATIONS 11 CITATIONS

[SEE PROFILE](#)



[Claudio Verrastro](#)

Comisión Nacional de Energía Atómica

33 PUBLICATIONS 30 CITATIONS

[SEE PROFILE](#)



[Lucio martinez garbino](#)

Comisión Nacional de Energía Atómica

6 PUBLICATIONS 4 CITATIONS

[SEE PROFILE](#)



[E. da Ponte](#)

Comisión Nacional de Energía Atómica

4 PUBLICATIONS 4 CITATIONS

[SEE PROFILE](#)

All content following this page was uploaded by [Martín Alberto Belzunce](#) on 16 May 2014.

The user has requested enhancement of the downloaded file. All in-text references [underlined in blue](#) are added to the original document and are linked to publications on ResearchGate, letting you access and read them immediately.

An Attenuated Projector for Iterative Reconstruction Algorithm of a High Sensitivity Tomographic Gamma Scanner

Martín Belzunce, *Member, IEEE*, Claudio Verrastro, Lucio Martínez Garbino, Esteban Venialgo, Elías da Ponte, Augusto Carimatto, Juan Alarcón, Daniel Estryk, and Isaac Marcos Cohen

Abstract—Tomographic Gamma Scanners are tools for nondestructive assay and characterization of nuclear waste drums. In these scanners, a three dimensional image of the activity distribution of every radioisotope stored in the drum is obtained by performing a single-photon emission tomography. AR-TGS is a novel architecture of tomographic gamma scanners that combines an HPGe detector with six NaI(Tl) detectors in order to achieve high-sensitivity. In this work, a projector for a 2D MLEM reconstruction algorithm of AR-TGS is presented. This projector models the geometry of the system, the collimator's response and the attenuation in the field of view by performing a ray-tracing with several lines of response per detector. The projector was evaluated with Monte Carlo simulations of different phantoms and with experimental measurements. The algorithm proved to be an accurate model of the acquisition process and was used to reconstruct data sets with different strategies, such as utilising matched and unmatched projector/backprojector pairs. The results showed that the use of this projector in image reconstruction considerably improved spatial resolution and image quality compared with an attenuated Siddon projector. The quantification properties of the algorithm for homogeneous and heterogeneous drums matrices were also analyzed.

Index Terms—Image reconstruction, NDA, projector, SPECT, tomographic gamma scanner.

I. INTRODUCTION

TOMOGRAPHIC GAMMA SCANNERS (TGS) are tools for nondestructive assay (NDA) and characterization of nuclear wastes. Traditional TGS systems combine a high resolution gamma ray spectroscopy based on an HPGe detector attached to a low spatial-resolution collimator, a transmission

source, and an image reconstruction algorithm to characterize radioisotope distributions [1]–[4]. The main goal of tomographic gamma scanning is to measure the amount and distribution of activity of each radioisotope inside a drum. The radioisotopes reside in a homogeneous or heterogeneous matrix of different materials, such as sludge, concrete, glass, etc. For this reason, a transmission scan is necessary to determine the attenuation map of the matrix. By performing an emission scan and using the attenuation map of the matrix, a three dimensional image of the activity distribution of each selected photo peak is obtained. The assay is carried out by dividing the waste drum volume into slices called segments. Each of them is scanned by shifting the detector-collimator in the axial direction. In order to generate a tomographic image of a segment, the drum under inspection must be rotated to obtain projections from angles evenly spaced between 0° and 360° . Each projection is sampled along several transverse positions. To achieve this, the detector must be moved along the transaxial direction.

In NDA of nuclear waste drums, the scan times are usually long, taking several hours to perform a tomographic assay of a drum. Therefore, it is important to increase the sensitivity of the scanners. The minimum detectable activity is also affected by this parameter. To reduce scanning times, scanners with multiple HPGe detectors were proposed before [5]. However, this geometry is quite expensive and needs a cooling system for all the detectors. As a consequence, we have proposed a TGS system, named AR-TGS (Argentine - Tomographic Gamma Scanner), that uses several NaI(Tl) detectors as a cost-effective solution to increase sensitivity [6]. The use of NaI detectors for tomographic gamma scanning was previously studied by Estep and Melton [7].

AR-TGS is a hybrid scanner with two types of radiation detectors. It has an HPGe detector that behaves as a Segmented Gamma Scanner (SGS) [8] and a detector head, that consists of six NaI(Tl) detectors and six collimators, to perform tomographic assays (Fig. 1). This number of detectors was selected in order to fully cover the diameter of the field of view (FOV) and increase the sensitivity of the tomographic system up to 50 times compared with a TGS with only one HPGe detector [6]. The high energy-resolution spectroscopy with the HPGe detector and the tomographic study, using the high-sensitivity and low energy-resolution detector head, are performed simultaneously. Each of the detectors has a collimator with an aspect

Manuscript received January 03, 2013; revised May 31, 2013; accepted January 19, 2014. Date of current version April 10, 2014. This work was supported by Comisión Nacional de Energía Atómica (CNEA) and Universidad Tecnológica Nacional (UTN), and in part by UTN Ph.D. fellowship to M. Belzunce.

M. Belzunce, C. Verrastro, L. Martínez Garbino, E. da Ponte, A. Carimatto, and J. Alarcón are with Comisión Nacional de Energía Atómica (CNEA), Gonzales y Aragón 15, Ezeiza, Buenos Aires, Argentina, and also with Universidad Tecnológica Nacional (UTN), Medrano 951, Ciudad Autónoma de Buenos Aires, Argentina (e-mail: belzunce@cae.cnea.gov.ar).

E. Venialgo and D. Estryk are with Comisión Nacional de Energía Atómica (CNEA), Gonzales y Aragón 15, Ezeiza, Buenos Aires, Argentina.

I. M. Cohen is with Departamento Ingeniería Química, Grupo IDeTQA, Universidad Tecnológica Nacional, Medrano 951, C1179AAQ, Ciudad Autónoma de Buenos Aires, Argentina.

Color versions of one or more of the figures in this paper are available online at <http://ieeexplore.ieee.org>.

Digital Object Identifier 10.1109/TNS.2014.2302454

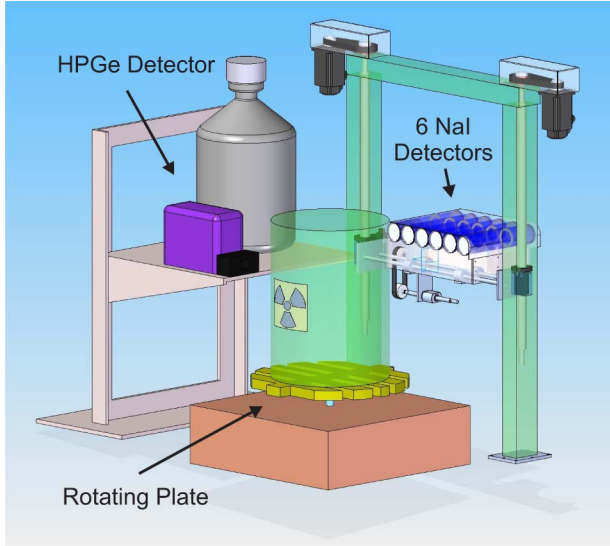


Fig. 1. Architecture of AR-TGS. An HPGe detector is used to perform high resolution spectroscopy and a head of six NaI(Tl) detectors to carry out the tomographic measurement.

ratio of 5:1, giving priority to sensitivity over spatial resolution. A scatter subtraction method is needed to reduce the scattered events coming from higher energy radioisotopes due to the low energy-resolution of the tomographic detectors. By visual inspection of the HPGe spectrum, it is verified that the energy window selected to reconstruct the spatial distribution of a specific radioisotope is not widely contaminated with another radionuclide that could not be observed in the energy spectrum of the tomographic detectors. When the mix of radioisotopes in a drum makes the net peak areas difficult to measure, a complex spectrum processing technique should be used, such as the gross count material basis set (GC-MBS) method [9].

Image reconstruction algorithms are an important component of tomographic imaging systems. Iterative reconstruction algorithms can generate superior images regarding quality, resolution and quantification, provided that a precise model of the acquisition process is utilized [10], [11]. This model is called projector and must take into consideration geometrical and physical factors. When performing tomographic assays of waste drums, both the wide collimators and the exponential attenuation of dense matrices have significant influence. Thus, these effects must be taken into account in order to be able to have quantitative images.

In this work, a projector for a 2D iterative reconstruction algorithm used in the AR-TGS is presented. This algorithm processes each segment as individual assays. The projector considers geometrical and physical factors, such as collimator aperture, septa penetration and gamma attenuation in the FOV. Since the focus of this work is on the emission image reconstruction, we have used modeled attenuation maps with the linear attenuation coefficients of the phantoms. The algorithm was evaluated performing an analysis of the spatial resolution and the accuracy of the activity quantification for simulated data of the AR-TGS scanner.

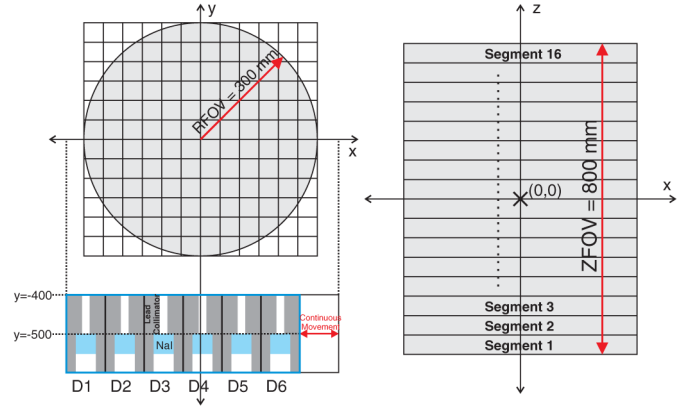


Fig. 2. AR-TGS geometric description of the tomographic scanner. It has cylindrical field of view with 16 segments in height and a radius of 300 mm. The external surface of each collimator is placed 400 mm away from the center of the FOV.

II. MATERIALS AND METHODS

A. AR-TGS

In the proposed system, the tomographic assay is executed with a detector head that has six NaI(Tl) crystals to increase its sensitivity. The HPGe detector is utilized to check that the radioisotope being processed is not widely contaminated with other radionuclides and to perform a global assay as in SGS systems.

Each of the six detectors consists of a $2'' \times 2''$ scintillator and a cylindrical lead collimator of 100 mm length, 100 mm diameter and a hole of 20 mm diameter. The collimator geometry was evaluated in a previous study [6] to comply with high sensitivity, admissible spatial resolution and good shielding for high energy gamma-rays. In order to improve spatial sampling and to measure the blind positions occupied by collimators, the head of six detectors has a continuous movement along the transverse position. The breadth of movement is equal to the width of a single detector and it takes five minutes for the mechanism to cover this distance.

The scanner has a cylindrical FOV of 800 mm height and 600 mm diameter to fulfill with the size of a 208 L waste drum. The FOV is divided into sixteen segments of 50 mm height. In Fig. 2 a geometrical description of the system is shown. The continuous sampling in the transverse axis is discretized into 60 transverse positions, 10 for each detector. In addition, the collected projections of the waste drum are grouped in angular steps of 6° . Therefore, each scan of a drum's segment produces a 60×60 sinogram.

B. GATE Simulations

Monte Carlo simulations of the acquisition process for different phantoms were performed using GATE [13]. Each run simulated the measurement of a single segment during 10 min. The simulated phantoms were:

- Several point sources phantom (upper left in Fig. 3). It consists of fifteen $100 \mu\text{Ci}$ point sources of ^{137}Cs distributed

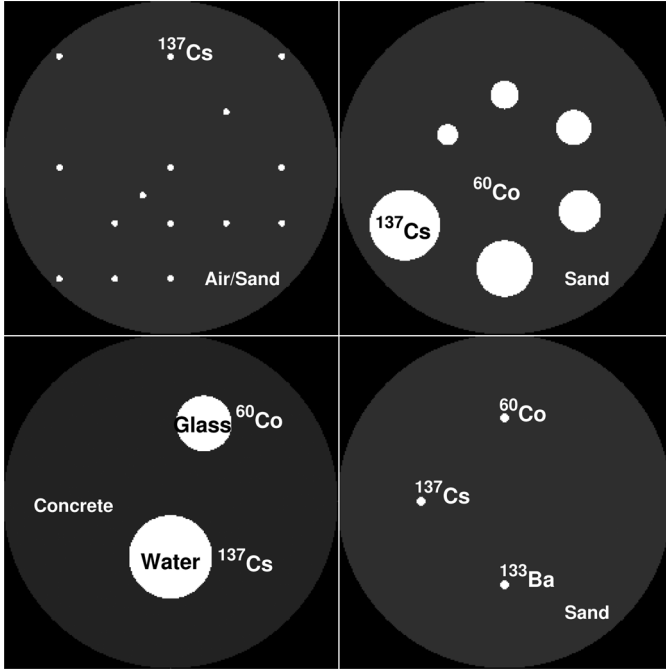


Fig. 3. Phantoms used in the Monte Carlo simulations to evaluate AR-TGS image reconstruction algorithm, in all of them the gray circle sets the limit of the drum and has a diameter of 600 mm. Upper left: several ^{137}Cs point sources in either air or sand. Upper right: resolution phantom of sand with ^{137}Cs rods and ^{60}Co in the background. Lower left: phantom with an heterogeneous matrix of concrete with two rods of water and glass. Lower right: three point sources of ^{133}Ba , ^{137}Cs and ^{60}Co in sand.

in a segment filled either with air or sand. In order to evaluate spatial resolution, different distances between point sources were used: 70.7 mm, 100 mm, 141.4 mm, 200 mm and 282.8 mm.

- Resolution phantom (upper right in Fig. 3). It is composed of six rods with distributed sources of ^{137}Cs in a uniform background of ^{60}Co . The rods have diameters of 38.1 mm, 50.8 mm, 63.5 mm, 76.2 mm, 101.6 mm and 127 mm. The phantom and the rods were 50 mm height. The activity concentration in the rods was $2 \mu\text{Ci/cc}$, while $0.5 \mu\text{Ci/cc}$ in the background. The matrix of this phantom consisted of sand.
- Heterogeneous matrix phantom (lower left in Fig. 3). The matrix of the segment is of concrete with two cylindrical rods of water and glass. The first rod has a diameter of 150 mm and a uniform source of ^{137}Cs with an activity concentration of $6.6 \mu\text{Ci/cc}$ inside. The second one has a uniform source of ^{60}Co with $9.1 \mu\text{Ci/cc}$ and its diameter is of 100 mm.
- Low Activity multi-radionuclide phantom (lower right in Fig. 3). It consists of three point sources of ^{133}Ba , ^{137}Cs and ^{60}Co in sand. The activity of each point source is $10 \mu\text{Ci}$ for a standard version of the phantom and $1 \mu\text{Ci}$ in its low activity model.

The sand used in the simulations was defined in GATE as silicon dioxide (SiO_2) with a density of 1.65 g/cm^3 , taking as reference the density of the sand used in the experiments with real data. The linear attenuation coefficient of the simulated sand

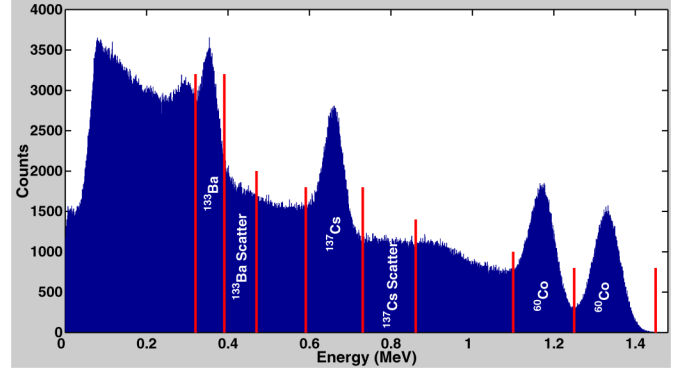


Fig. 4. NaI energy spectrum of the simulation of the phantom with ^{133}Ba , ^{137}Cs and ^{60}Co point sources in sand. The energy windows used for reconstruction and for scatter correction of each radioisotope are marked.

was 0.12 cm^{-1} and it was obtained by simulating a simple transmission experiment with a collimated ^{137}Cs point source and a known volume of sand. This simulation was validated with a measurement of the same transmission experiment.

For each simulated phantom a 2D sinogram was generated. In the phantoms with ^{137}Cs sources an energy window of 591-731 keV was used. For ^{60}Co , we used both photopeaks to produce the sinograms, with two energy windows of 1100-1250 keV and 1260-1500 keV. For ^{133}Ba , the higher energy photopeak was used with an energy window of 320-390 keV. In the simulations of phantoms with more than one radionuclide, the lower energy photopeaks were highly contaminated with scatter radiation from higher energy radioisotopes. To solve this, we applied a simple scatter correction method in which a scatter sinogram is obtained from an energy window next to the photopeak of interest (Fig. 4). Then a bin to bin subtraction is performed between the photopeak and the scatter sinograms and finally a corrected sinogram for reconstruction is obtained. If any bin becomes negative in the subtraction, it is forced to 0.

The method mentioned above is useful to reduce the background scatter generated by higher energy radioisotopes, however it does not take into account the scattered events from the radioisotope of interest that are inside the energy window. As a consequence, an overestimation of the activity values is usually observed. For this reason, we also used the triple energy window (TEW) method for scatter correction as proposed in [14]. In its implementation, we used two energy windows of 10 keV at each side of the photopeak energy window. For ^{60}Co , we applied this technique for each photopeak separately and then summed both results in a single sinogram.

In order to evaluate the system in a real environment, we added a background source to every simulation. To achieve this, we measured the background activity in the facility where AR-TGS will be used. The measurement was carried out using one NaI(Tl) detector with its collimator. With the measured energy spectrum, we generated an histogram source in GATE. We calibrated the activity of the source to get the same background energy spectrum for each detector when no other source is present. In Fig. 5, the measured and simulated energy spectrums are shown.

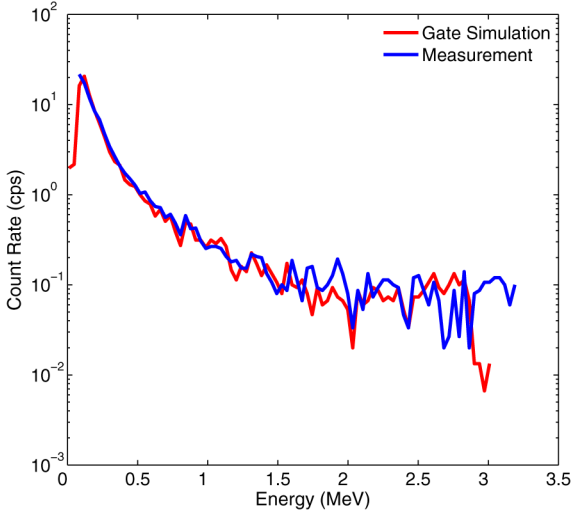


Fig. 5. Energy spectrum of the background activity measured in the facility where AR-TGS will be installed and the energy spectrum of a GATE simulation with the modeled background source.

C. Attenuated Cone of Response Projector

Images are reconstructed using a 2D MLEM (Maximum Likelihood Expectation Maximization) reconstruction algorithm [10], [12]:

$$x_j^{k+1} = \frac{x_j^k}{\sum_{i=1}^P a_{ij}} \cdot \sum_{i=1}^P \frac{a_{ij} \cdot b_i}{\sum_{j=1}^Q a_{ij} \cdot x_j^k} \quad (1)$$

where a_{ij} are the elements of the System Matrix Response (SMR) and are determined by the projector used, b_i are each of the P bins of the 2D sinogram and x_j^k are the Q pixels of the reconstructed image in the k th iteration.

A complete projector for AR-TGS, called Attenuated Cone of Response (ACOR), is presented in this work. The projector models the collimator's aperture by doing a multi-line ray-tracing. A similar strategy has already been developed by other authors [15]. In our algorithm, we use Siddon's algorithm [16], [17] to process each line instead of a fixed steps algorithm. Furthermore, the lines of response (LORs) are defined by joining fixed points on the detector surface to the points on the collimator hole (Fig. 6), rather than processing only the lines that go through the center of the collimator. Finally, we take into account the gamma penetration in the collimator by processing LORs that go through a short length of the collimator. To achieve this, an offset from the detector's edge is used to exclude the area of the detector that is well shielded but to also include the area where radiation can penetrate through the collimator. The amount of points on each surface and the length of the offset is a parameter of the projector. In this way, the low spatial resolution collimator is fully modeled.

To obtain quantified images, the projector must consider that the intensity detected from a source located in a pixel falls off with the square of the distance to the detector. Since our reconstruction algorithm is in bidimensional space, the number of LORs passing through a pixel in the multi-line ray tracing is

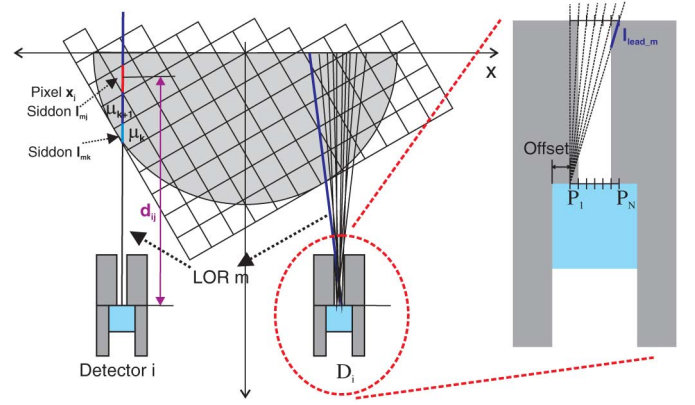


Fig. 6. Components of the Attenuated Cone of Response projector. For each detector's position i , several LORs are generated by joining points P_1 to P_N on the detector surface to every point on the collimator hole (magnified on right). Each LOR m is projected using the intersection length with each pixel j (l_{mj}), the attenuation coefficient of each pixel k (μ_k) and the distance from pixel j to detector i (d_{ij}).

only equivalent to the inverse of the distance [18]. Thus, an additional correction factor that falls off with the distance must be included to achieve a good approximation to the real model of the solid angle in a 2D reconstruction.

In addition, attenuation is considered in the ray-tracing algorithm. In single photon emission tomography (SPECT), attenuation correction is pixel dependent so it is not possible to apply it directly to the sinogram. For this reason, each LOR is attenuated during the ray-tracing [19] with the following equation:

$$AW_{mj} = e^{-\sum_{k=0}^j l_{mk} \cdot \mu_k} \quad (2)$$

where AW_{mj} is the attenuation weight for pixel j projected in the LOR m ; k is the index of every intersected pixel between the detector and the pixel j ; l_{mk} is the length in cm of the intersection segment between LOR m and pixel k ; and μ_k is the linear attenuation coefficient of pixel k in the attenuation map. The complete projector is described in equation (3).

$$a_{ij} = \sum_{m=1}^{N^2} l_{mj} \cdot \frac{1}{d_{ij}} \cdot e^{-\sum_{k=0}^j l_{mk} \cdot \mu_k} \cdot e^{-l_{lead_m} \cdot \mu_{lead}} \quad (3)$$

where a_{ij} is the system matrix response coefficient for pixel j and detector's position i , m is the index of all the LORs used in the Cone of Response for detector's position i and N is the number of points used on the detector surface and on the top of the collimator to generate them. For each point on the detector, N LORs are produced. Therefore, a total of N^2 LORs per sinogram bin are used. d_{ij} is the distance in cm from pixel j to detector i . The first exponential factor is the attenuation in the drum and the last is the attenuation in the collimator, where l_{lead_m} is the length in cm of the LOR m in the collimator's lead. In this work, ACOR was configured with $N = 30$ and an offset from the edge of the detector of 10 mm. Thus, the points on the detector's and collimator's surface have a separation of 1 mm. With such small step, the bias introduced by using equidistant points to sample the solid angle is negligible and, additionally,

the farthest pixels from the detector are intersected by at least one LOR.

D. Image Reconstruction

The simulated sinograms were reconstructed with MLEM using both Siddon and ACOR projectors. ‘Siddon projector’ here refers to the attenuated version of Siddon’s algorithm [19]. In this projector, a perfect collimator is considered, therefore only one straight LOR per detector position is computed.

The reconstructed images have a size of 60×60 pixels. For the attenuation correction, we used the theoretical attenuation maps of the phantom’s matrices. In the implementation, the system matrix was computed and stored previously to the reconstruction process. This was possible because of the small size of the SMR, which has 13 millions of elements.

The MLEM algorithm with ACOR projector has a slow convergent rate. For this reason, we decided to evaluate the use of an unmatched projector/backprojector pair [20]. In this strategy, a SMR is employed for the projector and another, different one, for the backprojector. The use of a full-modeled projector and a simple backprojector have been evaluated before with good results [21]. For this reason, we used ACOR as projector and the attenuated Siddon as backprojector.

We applied a smoothing filter after reconstruction to every image. In the case of MLEM with Siddon and with unmatched ACOR-Siddon projectors, images were very sensitive to Poisson noise, which increased considerably with iterations. Therefore, we also used a penalized MLEM [22] reconstruction for both cases. We used a median root prior implemented with the one step late strategy [23].

E. Activity Quantification

The reconstructed images are converted to activity concentration in $\mu\text{Ci/cc}$. To achieve this, we performed a simulation of a cylinder phantom with the size of the FOV with a uniformly distributed source of ^{137}Cs . A normalization sinogram and a conversion matrix from count rate to activity were computed using the simulation results. This conversion matrix is applied to every reconstructed image. When an image of other radioisotope is being reconstructed, an additional weight is used to compensate for the efficiency of the NaI detectors for that photopeak. The branching ratio of the radioisotope is also taken into account.

F. Acquisition with Real Data

A prototype of the AR-TGS was build in order to validate the system and test the image reconstruction algorithm with real data. The prototype consists of the six NaI(Tl) detectors and collimators and a rotation platform. The acquisition electronics was a 1024 channels multi-channel analyzer (MCA) with a time stamp to synchronize with the rotation movement.

We set up two experiments with a segment’s phantom and ^{137}Cs point sources placed in different locations. In the first essay, the first point source had 200 μCi and was placed in the center of the cylindrical segment, the second had 100 μCi and was placed 120 mm away from the center. In the second measurement, the same point sources were placed with a separation of 9 cm between them and a low activity point source (5 μCi) of ^{137}Cs was added more than 20 cm away from the others. In

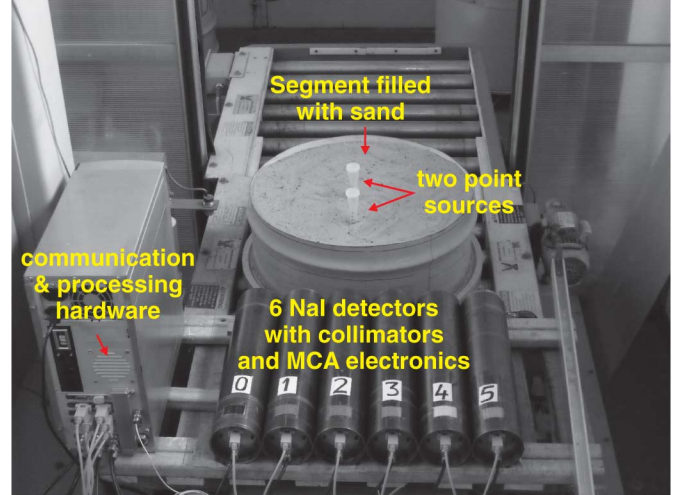


Fig. 7. Experimental measurement performed in the facility where AR-TGS is being built. The six NaI(Tl) detectors, with its collimator and MCA electronics, the processing hardware and the segment’s phantom filled with sand on the rotation platform are displayed in the image. The two inserts with point sources are also marked.

both cases, the segment was filled with sand with the attributes mentioned in the Gate Simulations section. The detector unit was shifted transversally in ten steps of 1 cm in order to emulate the continuous movement that it will be available in the scanner. The acquisition time for each detector head’s position was of one minute in order to have a total measurement time of 10 minutes. The use of ten transversal positions with six detectors allowed to build sinograms with the same size than the ones used for the simulated data. In Fig. 7, the set up of the first experiment can be observed.

III. RESULTS

A. Accuracy of the Projector

The Attenuated Cone of Response projector was contrasted with the Gate [13] simulations of each phantom. The projection of every phantom image using ACOR was compared to the GATE sinograms that were used as reference. The normalized root mean squared error (NRMSE) between the GATE and the projected sinograms was computed. The NRMS is the root mean square error between a projected sinogram and the reference sinogram, normalized to the mean value of the latter. Moreover, phantom images were projected with an attenuated Siddon projector in order to compare its performance with ACOR.

The Cone of Response projector proved to be an accurate model of the acquisition process of the AR-TGS. The comparison between the reference GATE sinograms and the projected ones with Siddon and ACOR are depicted in Fig. 8. The NRMS values for ACOR were lower than for the attenuated Siddon projector. The shape of the GATE sinograms matched with the ones projected with ACOR.

B. Reconstructed Images

All the GATE sinograms were reconstructed using the methods described in Materials and Methods. The MLEM

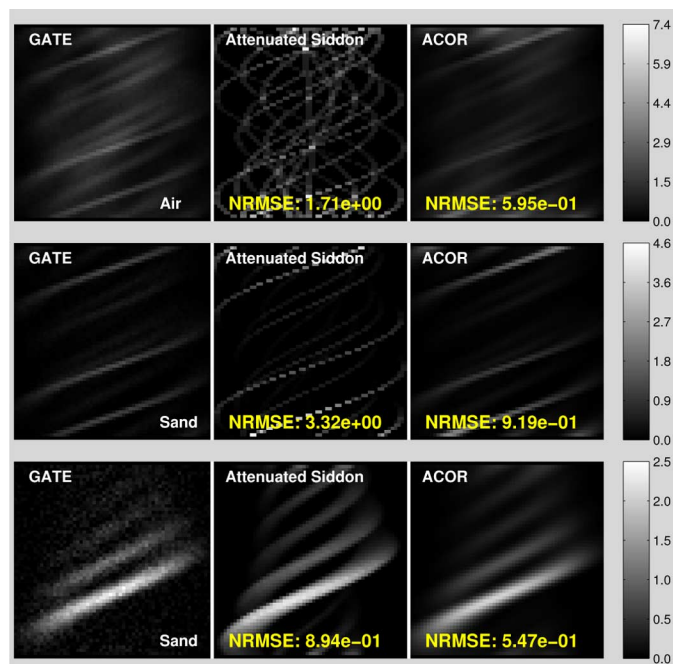


Fig. 8. Comparison of the GATE sinograms (left column) with the ones projected with Siddon (middle column) and ACOR (right column). On top it is the phantom with several point sources in air, in the middle row the same phantom but in sand and finally the resolution phantom in the lower row. The color scales are in counts per second (cps).

reconstructions were performed with 120 iterations and the triple window method was used for scatter correction. Fig. 9 shows the reconstructed images, using different projectors, of the several point sources phantom with matrices of air and sand. The images for the resolution phantom are also included.

The images obtained with MLEM using the unmatched ACOR-Siddon projector/backprojector pair had a better resolution and most of the point sources were clearly identified. The point sources that were 70 mm apart were barely isolated, indicating the limit for the resolution recovery with this method. However, the image of the resolution phantom was very noisy in the region of the smaller rods. The reconstructed images using MAP with Siddon and unmatched ACOR-Siddon projector/backprojector are depicted in Fig. 10.

The images reconstructed with matched ACOR showed better results in the resolution phantom. On the other hand, in the several point sources the sources were more blurred in the radial direction than with the unmatched reconstruction.

To analyze the convergence of each projector the log-likelihood was plotted in Fig. 11. Siddon projector converges quickly but to a lower likelihood value. The matched ACOR and the unmatched ACOR-Siddon methods attain similar likelihood values, but the unmatched strategy accelerated the convergence as it was expected.

In order to quantify the quality of the images, we used three metrics: the spatial resolution of a point source in different regions of the FOV, the total estimated activity for each reconstructed phantom and the activity recovery in the rods of the resolution and heterogeneous phantoms.

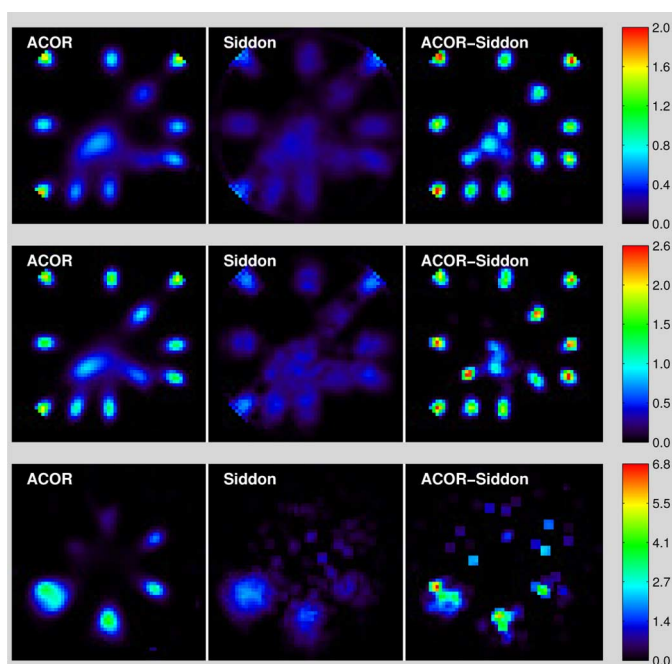


Fig. 9. Images reconstructed using different projectors. The color scales are in $\mu\text{Ci/cc}$. Upper row: reconstructed images of the several point sources phantom in air. Middle row: reconstructed images of the several point sources phantom in sand. Lower row: reconstructed images of the resolution phantom. Left column: images reconstructed with MLEM using ACOR. Middle column: images reconstructed with MLEM using Siddon. Right column: images reconstructed with MLEM using unmatched ACOR-Siddon projectors.

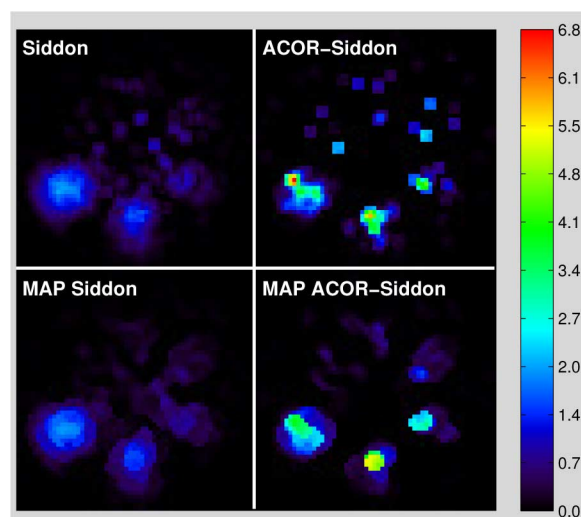


Fig. 10. Images reconstructed for the resolution phantom without and with penalization. The color scale is in $\mu\text{Ci/cc}$. Upper left: using Siddon projector and post-filtering. Lower left: using Siddon projector in a penalized MAP reconstruction. Upper right: images reconstructed with MLEM using unmatched ACOR-Siddon projectors. Lower right: images reconstructed with MLEM using unmatched ACOR-Siddon projectors in a penalized MAP reconstruction.

C. Spatial Resolution

For the several point sources in air phantom, the simulation was also processed considering one of the point sources at a

TABLE I
FWHM AND FWTM OF RECONSTRUCTED POINT SOURCES

Radial Position	FWHM						FWTM					
	Siddon		ACOR		ACOR-Siddon		Siddon		ACOR		ACOR-Siddon	
	radial	tangential	radial	tangential	radial	tangential	radial	tangential	radial	tangential	radial	tangential
0 mm	98 mm	94 mm	38 mm	37 mm	47 mm	48 mm	182 mm	181 mm	71 mm	69 mm	68 mm	67 mm
71 mm	91 mm	91 mm	36 mm	37 mm	40 mm	43 mm	176 mm	178 mm	69 mm	68 mm	55 mm	64 mm
100 mm	92 mm	92 mm	34 mm	37 mm	43 mm	42 mm	161 mm	178 mm	65 mm	69 mm	60 mm	62 mm
200 mm	97 mm	68 mm	37 mm	28 mm	44 mm	44 mm	167 mm	119 mm	67 mm	53 mm	67 mm	58 mm
223 mm	80 mm	65 mm	35 mm	29 mm	41 mm	39 mm	163 mm	126 mm	63 mm	56 mm	67 mm	55 mm
282 mm	30 mm	54 mm	22 mm	23 mm	32 mm	37 mm	81 mm	112 mm	37 mm	43 mm	42 mm	55 mm

TABLE II
TOTAL ACTIVITY ESTIMATION OF RECONSTRUCTED IMAGES

Phantom	Activity	Higher Window Subtraction				Triple Window			
		ACOR		ACOR-Siddon		ACOR		ACOR-Siddon	
		Activity	error	Activity	error	Activity	error	Activity	error
Point Sources in Sand	1500 μCi	1827 μCi	21.8 %	1849 μCi	23.3 %	1471 μCi	-1.9 %	1474 μCi	-1.7 %
Resolution Phantom (^{137}Cs)	3164 μCi	3864 μCi	22.1 %	3867 μCi	22.2 %	2887 μCi	-8.7 %	2986 μCi	-5.6 %
Resolution Phantom (^{60}Co)	6257 μCi	6939 μCi	10.9 %	7020 μCi	12.2 %	5543 μCi	-11.4 %	5518 μCi	-11.8 %
Heterogeneous Matrix (^{137}Cs)	5857 μCi	7350 μCi	25.5 %	7470 μCi	27.5 %	6110 μCi	4.3 %	6221 μCi	6.2 %
Heterogeneous Matrix (^{60}Co)	3589 μCi	4210 μCi	22.5 %	3550 μCi	21.25 %	2445 μCi	-16.4 %	2414 μCi	-17.5 %

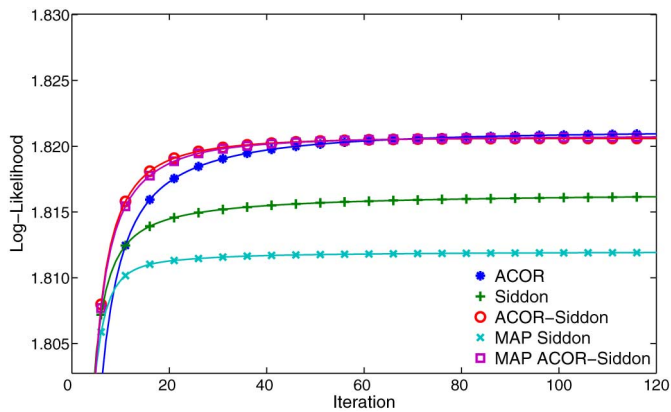


Fig. 11. Log-likelihood values scaled by 10^6 of the MLEM reconstruction for the phantom with several point sources in sand. The convergence rate of each projector is depicted. Asterisks: ACOR projector. Plus Signs: Siddon projector. Circles: unmatched ACOR-Siddon projectors. Crosses: Siddon projector in MAP reconstruction. Squares: unmatched ACOR-Siddon projectors in MAP reconstruction.

time. Thus, we could perform an analysis of the spatial resolution in different regions of the FOV. To achieve this, we computed the full-width at half-maximum (FWHM) and full-width at tenth-maximum (FWTM) in both radial and tangential directions for each reconstructed point source. The obtained values of FWHM and FWTM are presented in Table I.

The point source placed in the center of the FOV had a FWHM of $98 \text{ mm} \times 94 \text{ mm}$ in two perpendicular directions when the image was reconstructed using MLEM with the attenuated Siddon algorithm; on the other hand, a resolution of $38 \text{ mm} \times 37 \text{ mm}$ was achieved when using MLEM with ACOR projector and $47 \text{ mm} \times 48 \text{ mm}$ with unmatched ACOR-Siddon projectors. Therefore, the use of ACOR projector improved spatial resolution more than twice. As expected in SPECT systems, the center of the FOV was the region with lower spatial resolution.

D. Activity Estimation

All the reconstructed images were quantified in activity concentration using the calibration matrix described previously. In Table II, the total activity measured in each reconstructed image is shown and compared with the activity of the phantoms. There is also a comparison between the upper window subtraction and the TEW methods for scatter correction. To evaluate the effectiveness of the attenuation correction of ACOR projector, we observed the quantification results in the phantoms with the heterogeneous and sand matrices. The quantification error was less than 12% in four of the five phantoms when the TEW scatter correction method was used. For the background subtraction method, an overestimation of activity of around 20% was observed. Thus, the TEW method proved to be a meaningful better solution for scatter correction.

The use of the penalized MAP algorithm, instead of a simple MLEM, produced negligible changes in the estimated activities. For that reason, in Table II we only included the results for the images reconstructed with MLEM.

In addition, we evaluated the measured activity for each of the point sources used in the spatial resolution section (Table III). To achieve this, we processed the several point sources phantom in air and sand, considering only one point source at a time and performing the TEW method for scatter correction. The use of ACOR projector achieved better quantification results in this analysis. The point sources near the center of the FOV had an increasing bias in the estimated activity.

E. Activity Recovery

For the heterogeneous matrix phantom and resolution phantom, we computed the percent of activity recovery for each rod. This parameter is defined by the rate between the estimated activity in a region of interest (ROI) with the size and location of the rod, and the total activity simulated in that rod.

The values of the percent of activity recovery for different rod sizes are presented in Table IV. The use of ACOR projector achieved a significant better activity recovery than the Siddon

TABLE III
ACTIVITY ESTIMATION OF RECONSTRUCTED POINT SOURCES

Radial Position	Air Matrix				Sand Matrix			
	ACOR		ACOR-Siddon		ACOR		ACOR-Siddon	
	Activity	error	Activity	error	Activity	error	Activity	error
0 mm	95.7 μCi	-4.3 %	109.2 μCi	9.2 %	121.1 μCi	21.1 %	129.7 μCi	29.7 %
71 mm	95.3 μCi	-4.7 %	104.8 μCi	4.8 %	115.7 μCi	15.7 %	122.7 μCi	22.7 %
100 mm	96.2 μCi	-3.8 %	105.4 μCi	5.4 %	110.1 μCi	10.1 %	114.5 μCi	14.5 %
200 mm	99.5 μCi	-0.5 %	109.2 μCi	9.2 %	106.4 μCi	6.4 %	116.1 μCi	16.1 %
223 mm	100.5 μCi	0.5 %	112.4 μCi	12.4 %	107.6 μCi	7.6 %	123.4 μCi	23.4 %
282 mm	106.9 μCi	6.9 %	115.7 μCi	15.7 %	106.8 μCi	6.8 %	113.4 μCi	13.4 %

TABLE IV
ACTIVITY RECOVERY IN RODS OF HETEROGENEOUS MATRIX AND
RESOLUTION PHANTOM

Phantom	Rod Size	Siddon	ACOR	ACOR-Siddon	MAP
					ACOR-Siddon
Resolution	38.1 mm	6.1 %	9.4 %	4.6 %	7.8 %
	50.8 mm	7.4 %	26.8 %	8.1 %	23.3 %
	63.5 mm	11.8 %	37.7 %	8.3 %	22.3 %
	76.2 mm	30.1 %	65.1 %	67.3 %	71.6 %
	101.6 mm	47.8 %	75.6 %	79.1 %	81.5 %
	127 mm	64.1 %	84.5 %	84.1 %	86.1 %
Heterogeneous Matrix	100 mm	56.9 %	95.3 %	87.0 %	89.9 %
	150 mm	39.5 %	72.1 %	77.4 %	77.6 %

projector. For the rod of 76.2 mm diameter similar values were obtained with matched and unmatched strategies. But for smaller rods, the matched ACOR outperformed the unmatched ACOR/Siddon projector despite having the same performance in total activity estimation (Table II). This worse performance of the unmatched ACOR/Siddon projector agrees with the images of Fig. 9, where there are noisy regions where it should be located the smaller rods.

F. Multi-Radioisotope Images

The phantom with three point sources of ^{133}Ba , ^{137}Cs and ^{60}Co in sand was reconstructed for each photopeak using the TEW scatter correction method with a scatter energy window of 30 keV. The sinograms of each radionuclide were reconstructed separately. For the 10 μCi assay, the estimated activity for each respective source was of 9.5 μCi , 6.8 μCi and 9.8 μCi with ACOR; and of 9.7 μCi , 12.5 μCi and 17.2 μCi with Siddon. For the 1 μCi assay (Fig. 12), the respective estimated activities were 1.2 μCi , 0.7 μCi and 1.5 μCi with ACOR; and 2.1 μCi , 2.6 μCi and 3.9 μCi with Siddon. This assay shows that a point source of 1 μCi is detectable for scans of 10 minutes per segment and for the environment conditions of our facility.

In these assays, the Poisson noise in the sinograms and the influence of the background source increased the error in the activity estimation. In addition, the scatter correction increments the noise due to the subtraction of bins with low counts. The use of Siddon projector and of unmatched ACOR-Siddon projector/backprojector generated noisier images and with more artifacts than ACOR (Fig. 12). To quantify this performance, we computed the rate between the activity in a ROI of 10 cm diameter centred in each point source and the total activity in the image. For the ^{133}Ba and ^{60}Co images, the matched ACOR projector achieved a 50% of the activity in the ROI, while the other two methods accomplished a 35%. For the ^{137}Cs images, ACOR obtained a 35% of activity recovery against a 30% in the

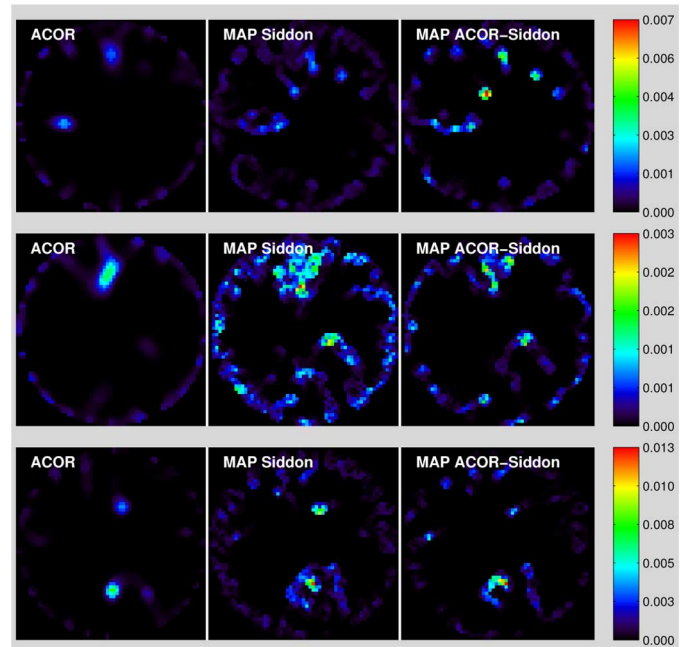


Fig. 12. Images reconstructed of the simulation with three 1 μCi point sources of ^{133}Ba , ^{137}Cs and ^{60}Co using MLEM with ACOR (left column), MAP with Siddon (middle column) and MAP with unmatched ACOR-Siddon (right column) projector. In the top row, the image for ^{137}Cs , in the middle for ^{60}Co and in the bottom row for ^{133}Ba photopeak. The color scales are in $\mu\text{Ci/cc}$.

other two methods. The worse performance of the ^{137}Cs is due to the contamination of the photopeak with the scattered radiation from the ^{60}Co source, as it is observed in the first row of Fig. 12.

G. Experimental Data

In the reconstruction of the first experimental measurement (top images in Fig. 13), the use of ACOR permitted to identify both point sources placed in the sand phantom. The difference of intensity between both point sources was also appreciated. We measured the activity in two ROIs with 14 cm diameter centred in each point source. For ACOR we got 188 μCi in the central point source and 103 μCi in the second one.

In the second assay, a ROI of only 8 cm diameter was used to measure the two point sources with higher activity in order to not overlap them. The measured activity was 91 μCi for one of the point sources and 172 μCi in the other one. For the low activity (5 μCi) point source, an activity of 4.2 μCi was measured using a ROI of 14 cm diameter. A logarithmic scale was used in the image of the Fig. 13 (bottom row) to allow the visualization of the three point sources due to the big difference in their

TABLE V
ACTIVITY ESTIMATION OF RECONSTRUCTED POINT SOURCES WITH EXPERIMENTAL DATA

Phantom	Point Sources Nominal Activity	ACOR		MAP Siddon		MAP ACOR-Siddon	
		Activity	error	Activity	error	Activity	error
Two Point Sources	102 μCi	103 μCi	1.0 %	92 μCi	-9.8 %	108 μCi	5.9 %
	201 μCi	188 μCi	-6.5 %	139 μCi	-30.8 %	187 μCi	-7.0 %
Three Point Sources	102 μCi	91 μCi	-5.5 %	59 μCi	-42.1 %	91 μCi	-5.5 %
	201 μCi	172 μCi	-14.4 %	103 μCi	-48.8 %	174 μCi	-13.4 %
	5.1 μCi	4.2 μCi	-17.6 %	4.1 μCi	-19.6 %	4.2 μCi	-17.6 %

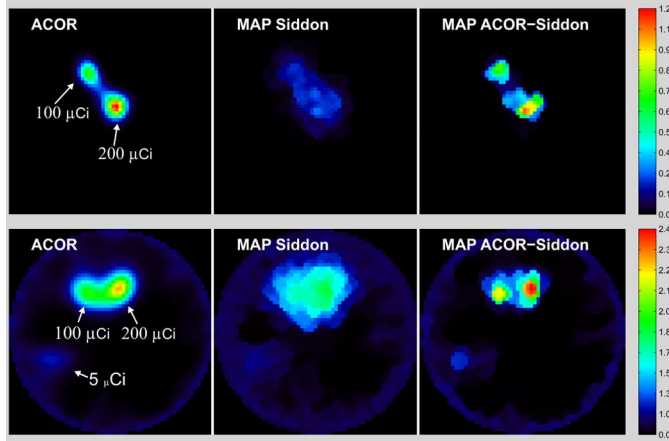


Fig. 13. Images reconstructed for the two experimental measurements using MLEM with ACOR (left), Siddon (middle) and unmatched ACOR-Siddon (right) projectors. In the top row, an assay with two point sources with 100 μCi and 200 μCi . In the bottom row, a point source pf 5 μCi was also included. The color scale is in $\mu\text{Ci/cc}$.

activities. The values of estimated activity for each point source of the two experiments are presented in Table V.

IV. DISCUSSION AND CONCLUSIONS

The use of the Attenuated Cone of Response projector in the MLEM reconstruction, for the AR-TGS gamma scanner, has shown to improve remarkably the spatial resolution and activity recovery of the system. Despite the low resolution collimator, a spatial resolution of less than 40 mm FWHM can be achieved with this image reconstruction algorithm. Good image quality and quantification was achieved in both not attenuating and attenuating materials. We must remark that the use of transmission scans instead of the simulated attenuation maps would introduce noise in the images and increase the error in the activity estimation. The use of ACOR in both matched and unmatched strategies outperformed attenuated Siddon projector in activity estimation and image resolution.

The use of an unmatched pair of projectors, with ACOR as forward projector and attenuated Siddon as backprojector, combined with a one step late penalization using a median root prior, proved to be a good strategy to accelerate the convergence of MLEM algorithm. In addition, it produced better results than matched ACOR for the phantom with several point sources. A one ray backprojector seems to enhance spatial changes in the activity and for this reason the point sources could be identified easier than with ACOR backprojector. On the other hand, this enhancement effect increases the noise and the artifacts when the simulated phantoms were filled with sand and sinograms

had fewer counts, as it was observed in the resolution phantom and the low activity assays. This suggests that the unmatched projectors could be a good option only in acquisitions with low Poisson noise, including assays of low activity drums but with long scans. The acceleration of the convergence rate and the reduction of the total computational load achieved with the unmatched approach could be important in an extension of ACOR to be used in a three dimensional reconstruction.

In the center of the FOV a decrease of the spatial resolution and intensity was observed, especially in the phantom with distributed sources. This is a common issue in SPECT systems, where the center of the FOV is the region with lowest spatial resolution. The decrease of intensity in the center of the FOV is a consequence of partial volume effect due to low spatial resolution.

An experimental verification of the tomographic system and the image reconstruction algorithm was achieved by performing two measurements using a prototype with the NaI detector head. In this case, the use of ACOR also resulted in a better spatial resolution and as a consequence the point sources located in the phantom were identified. Moreover, a low activity point source was detected in one of the measurements due to the good sensitivity of the system.

Finally, the algorithm improved the image quality in low activity measurements. The minimum detectable point source was of 1 μCi in a simulated segment's assay of 10 min that took into account the background activity of our facility. Therefore, with ACOR the sensitivity of the AR-TGS can be improved compared to using a simpler projector.

REFERENCES

- [1] R. Estep, D. Miko, S. Melton, and M. Rawool-Sullivan, *A Demonstration of the Gross Count Tomographic Gamma Scanner (GC-TGS) Method for Nondestructive Assay of Transuranic Waste*, Los Alamos National Laboratory, 1998.
- [2] R. Venkataraman and M. Villani *et al.*, "An integrated tomographic gamma scanning system for non-destructive assay of radioactive waste," *Nucl. Instrum. Methods Phys. Res. A*, vol. 579, pp. 375–379, 2007.
- [3] D. C. Camp, H. E. Martz, and G. P. Robertson *et al.*, "Nondestructive waste-drum assay for transuranic content by gamma-ray active and passive computed tomography," *Nucl. Instrum. Methods Phys. Res. A*, vol. 495, pp. 69–83, 2002.
- [4] C.-J. Chang and S. Anghaie, "Iterative reconstruction and statistical optimization for the nondestructive assay of distributed gamma source in a large nuclear waste container," *IEEE Trans. Nucl. Sci.*, vol. 45, no. 2, pp. 146–53, Apr. 1998.
- [5] R. T. Bernardi, "TRU drum NDE and NDA with the waste inspection tomography mobile trailer," in *Proc. Waste Management Conf.*, Tucson, AZ, USA, 1999.
- [6] E. Venialgo, M. Belzunce, and C. Verrastro *et al.*, "Analysis and comparison of tomographic gamma scanner (TGS) architectures for nuclear waste characterization systems," in *Proc. MRS*, 2012, vol. 1475.

- [7] R. J. Estep and S. Melton, "Using NaI detectors for tomographic gamma scanning," in *Proc. 5th Nondestructive Assay and Nondestructive Examination Waste Characterization Conf.*, Salt Lake City, UT, USA, 1997.
- [8] A. Bosko and G. Geurkov *et al.*, "Advanced approach for calibration of the segmented gamma scanner for the radioassay of drummed waste," in *Proc. Nuclear Science Symp. Conf. Rec.*, Oct. 2006, pp. 212–213.
- [9] R. Estep, M. Rawool-Sullivan, and D. Miko, "A method for correcting NaI spectra for attenuation losses in hand-held instrumentation applications," *IEEE Trans. Nucl. Sci.*, vol. 45, no. 3, pp. 1022–28, Jun. 1998.
- [10] K. Lange and R. Carlson, "EM reconstruction algorithms for emission and transmission tomography," *J. Comput. Assist. Tomogr.*, vol. 8, pp. 306–16, 1984.
- [11] J. A. Reader, A. Visvikis, and K. Erlandsson *et al.*, "Intercomparison of four reconstruction techniques for positron volume imaging with rotating planar detectors," *Phys. Med. Biol.*, vol. 43, pp. 823–34, 1999.
- [12] L. A. Shepp and Y. Vardi, "Maximum likelihood reconstruction for emission tomography," *IEEE Trans. Med. Imag.*, vol. MI-1, no. 2, pp. 113–122, 1982.
- [13] S. Jan, G. Santin, and D. Strul *et al.*, "GATE: A simulation toolkit for PET and SPECT," *Phys. Med. Biol.*, vol. 49, pp. 4543–4561, 2004.
- [14] K. Ogawa, Y. Harata, and T. Ichihara *et al.*, "A practical method for position-dependent Compton-scatter correction in single photon emission CT," *IEEE Trans. Med. Imag.*, vol. 10, no. 3, pp. 408–412, 1991.
- [15] D. Goodman, J. A. Jackson, H. E. Martz, and G. P. Roberson, "Active and passive computed tomography algorithm with a constrained conjugate gradient solution," in *Proc. 6th Nondestructive Assay Waste Characterization Conf.*, Salt Lake City, UT, USA, 1998.
- [16] R. L. Siddon, "Fast calculation of the exact radiological path for a three-dimensional CT," *J. Med. Phys.*, vol. 12, no. 2, pp. 252–255, 1985.
- [17] F. Jacobs, E. Sundermann, and B. De Sutter *et al.*, "A fast algorithm to calculate the exact radiological path through a pixel or voxel space," *Comp. Inf. Tech.*, vol. 6, no. 1, pp. 89–94, 1998.
- [18] G. K. Loudos, "An efficient analytical calculation of probability matrix in 2D SPECT," *Comput. Med. Imag. Graph.*, vol. 32, no. 2, pp. 83–94, 2008.
- [19] G. T. Gullberg *et al.*, "An attenuated projector-backprojector for iterative SPECT reconstruction," *Phys. Med. Biol.*, vol. 30, no. 8, pp. 799–816, 1985.
- [20] G. L. Zeng and G. T. Gullberg, "Unmatched projector/backprojector pairs in an iterative reconstruction algorithm," *IEEE Trans. Med. Imag.*, vol. 19, no. 5, pp. 548–555, 2000.
- [21] A. Welch and G. T. Gullberg, "Implementation of a model-based nonuniform scatter correction scheme for SPECT," *IEEE Trans. Med. Imag.*, vol. 16, no. 6, pp. 717–726, 1997.
- [22] P. J. Green, "Bayesian reconstructions from emission tomography data using a modified EM algorithm," *IEEE Trans. Med. Imag.*, vol. 9, no. 1, pp. 84–93, 1990.
- [23] S. Alenius and U. Ruotsalainen, "Bayesian image reconstruction for emission tomography based on median root prior," *Eur. J. Nucl. Med.*, vol. 24, no. 3, pp. 258–265, 1997.